TAS Journal, vol. 8, n. 3, p. 20
ISSN 2595-1521
SEPTEMBER 2024
carvalho@ipen.br

Predictive Diagnosis of Research Reactor Primary Pump Failures Using Artificial Neural Network and Vibration Data

CARVALHO, M.R.*; DIAS, M. S.*§; POVEDA, P. F.†; DE MESQUITA, R. N.*§.

Instituto de Pesquisas Energéticas e Nucleares, São Paulo, Brasil. §Universidade de São Paulo, São Paulo, Brasil †Instituto Federal de Educação Ciência e Tecnologia de São Paulo, São Paulo, Brasil.

Abstract. Neural networks are seldom employed in research nuclear reactors, particularly regarding applications involving vibration measurements. The existence of a vibration database, combined with expert analysis of these data, inspired the development of an artificial intelligence technique designed to automate the fault diagnosis process in the pumps of the IEA-R1 reactor. A new predictive diagnostic method for identifying failures in the primary cooling circuit pumps of the IEA-R1 research nuclear reactor is proposed. An Artificial Neural Network (ANN) is applied to the raw pump vibration signals both in the time and frequency domain. The Neural Network architecture is a feedforward network with 12 inputs employing a sigmoid transfer function and softmax in the output layer. The effectiveness of the proposed method is validated and compared with failure history during scheduled pump maintenance. The results fully agree with the neural network predictions.

Keywords. *Feedforward Neural Network, Predictive Diagnostic, Research Nuclear Reactor, Primary Cooling Circuit Pumps, Vibration Analysis, Failures Classifier.*

Introduction. The IEA-R1 nuclear research reactor is the first of its kind in the southern hemisphere. Crafted by the esteemed American entity, Babcock & Wilcox Co., the reactor achieved its inaugural criticality, boasting a power of 2 MW, on September 16, 1957. It is situated at IPEN (Instituto de Pesquisas Energéticas e Nucleares) on the campus of the University of São Paulo in São Paulo, Brazil.

During the latter part of the twentieth century, the reactor underwent a series of upgrades intended to enhance its power to 5 megawatts. In an effort to reduce the likelihood of a Loss of Coolant Accident (LOCA) precipitated by the rupture of piping within the primary circuit, attributable to the disengagement of the pump's inertia disk, a Vibration Monitoring System (VMS) was implemented in 1995. Presently, this VMS is non-operational, which has motived the development of a novel approach towards predictive monitoring.

doi.org/10.32640/tasj.2024.6.20

TAS Journal, vol. 8, n. 3, p. 20
ISSN 2595-1521
SEPTEMBER 2024
carvalho@ipen.br

Generally, the process of intelligent diagnosis in vibration analysis involves introducing known inputs into 'black boxes', which subsequently generate outputs corresponding to machine faults. ANNs are well-suited for this task and are extensively employed as an artificial intelligence tool for diagnosing faults in machinery (Table 1). Through the use of such a tool, maintenance personnel are relieved from the necessity of comprehending or managing the internal workings of a neural network. Their responsibility lies solely in inputting the pertinent data into the network, which is then trained to diagnose faults.

The intrinsic learning capability of ANNs enables them to model complex nonlinear systems, facilitating the accurate approximation of real-world fault diagnostics. These techniques are coupled with signal analysis methods to classify and quantify faults in various machine components, including bearings, gearboxes, rotors, turbines, motors, and fans. The identified faults encompass issues such as misalignment, imbalance, cracks, friction, and clearance.

Table 1 provides an updated summary of the various types of ANNs used and their applications in diagnosing faults in rotating machine components. The numbers in the table correspond to bibliographic references, serving as sources for information about the diverse ANNs and their respective applications.

The blue columns showcase references to different types of neural networks and their applications in diagnosing machine faults. The orange and green columns aim to underscore that, while ANNs have been applied in power Nuclear Power Reactors (NPR), their consolidation in Nuclear Research Reactors (NNR), remains incipient. Pertaining to NNR, the sole identified effort (HAGGAG; ADLY; ZAKY, 2022) is associated with the Coordinated Research Project (CRP) sponsored by the International Atomic Energy Agency (IAEA), titled Condition Monitoring and Incipient Failure Detection of Rotating Equipment in Research Reactors and On-Line Monitoring of Instrumentation in Research Reactors (2016-2018) (INTERNATIONAL ATOMIC ENERGY AGENCY, 2017). This initiative seeks to transfer technologies from power nuclear reactors to benefit research reactors.

In the IEA-R1 reactor, pump fault diagnosis is implemented using data from accelerometers, through specific features. Both the feature extractors and the neural networks were implemented in Matlab (THE MATHWORKS INC., 2021). The ANN used for this study was a simple 2-layer Perceptron using backpropagation.

doi.org/10.32640/tasj.2024.6.20

TAS Journal, vol. 8, n. 3, p. 20
ISSN 2595-1521
SEPTEMBER 2024
carvalho@ipen.br

Table 1 - ANNs Applied in the Diagnosis Faults;

	Gear	Bearings	Rotor	Turbine	Motor	Pump	NPR	NRR
Backpropagation Neural Network (BNN)					(GLOWACZ; GLOWACZ, 2018)			
Fuzzy Neural Network			(XU et al., 2020)					
Generative Adversarial		(TAO et al., 2020)						
Deep Neural Network	(LI; PANG; YANG, 2019)							
Spiking Neural Network		(ZUO et al., 2021)						
Generalized Regression			(IANNACE; CIABURRO; TREMATERRA, 2019)					
Recursive Least Square Backpropagation	(LU et al., 2020)	(LU et al., 2020)	(LU et al., 2020)				(ZHAO et al., 2020a)	
Differentiated Probabilistic Neural Network						(WANG; LU; ZHOU, 2018)		
Recurrent Neural Network		(LIU et al., 2018)					(EL-SEFY et al., 2021),(DURRANT; LEONTIDIS; KOLLIAS, 2019)	
Convolutional		(HOANG; KANG, 2019)	(HOANG; KANG, 2019)		(GARCIA-BRACAMONTE et al., 2019)		(EL-SEFY et al., 2021),(DURRANT; LEONTIDIS; KOLLIAS, 2019)	
Feed Forward Network		(SAUFI et al., 2018)		(ALBLAWI, 2020)			(EL-SEFY et al., 2021),(ZHAO et al., 2020b)	(HAGGAG; ADLY; ZAKY, 2022)
Multi layer Perceptron	(KELEŞOĞLU; KÜÇÜK; DEMETGÜL, 2020)	(ABDISA; W. T.; HARD, 2019)			(KHOUALDIA et al., 2021),(HOU et al., 2020)	(AL TOBI et al., 2022)		
Radial Based Networks	(LI et al., 2018)	(JIN et al., 2020)			(MARTÍNEZ-MORALES; PALACIOS-HERNÁNDEZ; CAMPOS-DELGADO, 2018)			
Long-short-term Memory (LSTM)							(EL-SEFY et al., 2021)	
NonLinear AutoRegressive (NLAR)							(SIANO; PANZA, 2018)	

Historical Retrospective

IEA-R1 Cooling Circuit. The IEA-R1 nuclear research reactor has a pool-type configuration, utilizing light water for cooling and moderation, supplemented by graphite reflectors, the reactor's pivotal attributes are shown in Figure 1.

doi.org/10.32640/tasj.2024.6.20

TAS Journal, vol. 8, n. 3, p. 20
ISSN 2595-1521
SEPTEMBER 2024
carvalho@ipen.br

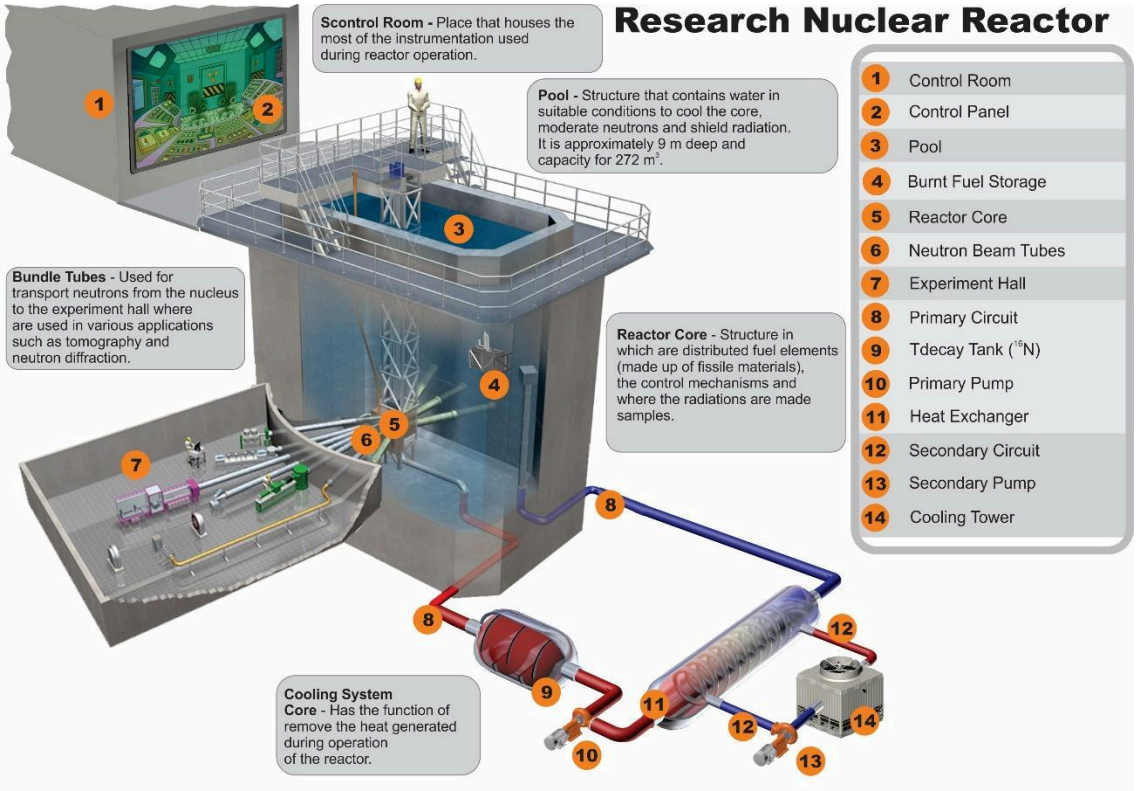

Figure 1 – IEA-R1 Reactor - Main components of the research nuclear reactor IEA-R1

The reactor cooling system was designed with demanding safety as first goal. This includes two pumps and two pipes for the primary circuit, as well as two pumps and two pipes for the secondary circuit. Additionally, the system contains two heat exchangers and two cooling towers, ensuring a robust and fail-safe configuration. A comprehensive overview of the IEA-R1 reactor cooling circuit is depicted in Figure 2.

doi.org/10.32640/tasj.2024.6.20

TAS Journal, vol. 8, n. 3, p. 20
ISSN 2595-1521
SEPTEMBER 2024
carvalho@ipen.br

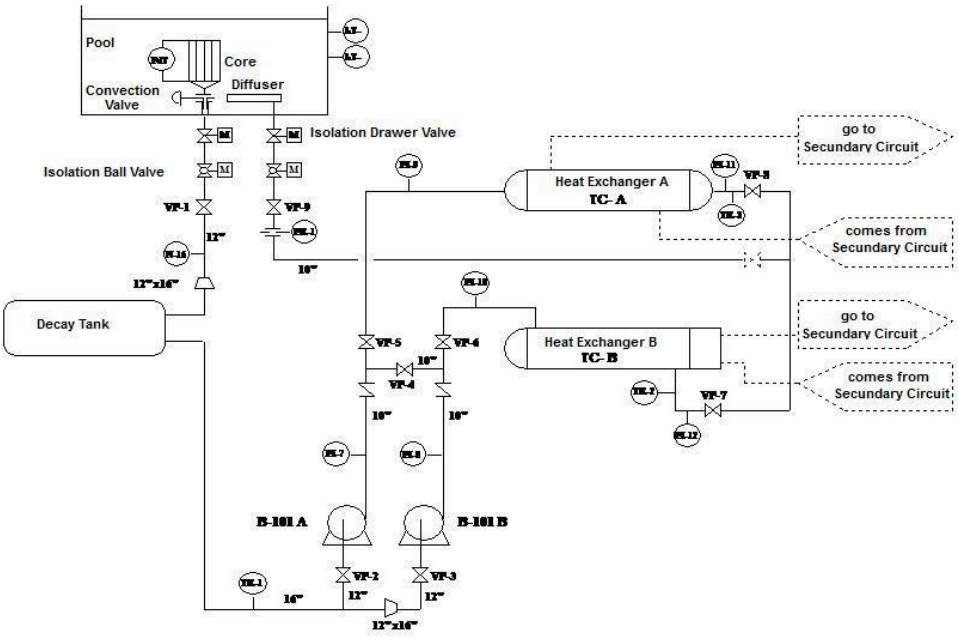

Figure 2 – Reactor Cooling Circuit - Flowchart of the primary cooling circuit of the reactor IEA-R1

The primary pumps are powered by 100 HP electric motors operating at a speed of 1760 rpm. Equipped with inertia wheels boasting a diameter of 650 mm and a width of 210 mm, with an approximate weight of 550 kg, the pumps couplings between the pump-wheels-drivers exhibit flexibility.

Signal Acquisition System. From the signal of accelerometers installed in the primary pumps, the VMS accumulates and processes vibration data through Root Mean Square (RMS) values and Power Spectrum. This RMS and spectrum are then examined and compared against a baseline to detect the initiation of equipment degradation or potential failure.

The condition monitoring of the primary pumps involves a thorough analysis of various screens displaying RMS values and Power Spectrum at each vibration measurement points. A comparison is made with machine reference levels derived from operational experience, maintaining values lower than established vibration measurement standards (INTERNATIONAL ORGANIZATION FOR STANDARDIZATION, 2016).

doi.org/10.32640/tasj.2024.6.20

TAS Journal, vol. 8, n. 3, p. 20
ISSN 2595-1521
SEPTEMBER 2024
carvalho@ipen.br

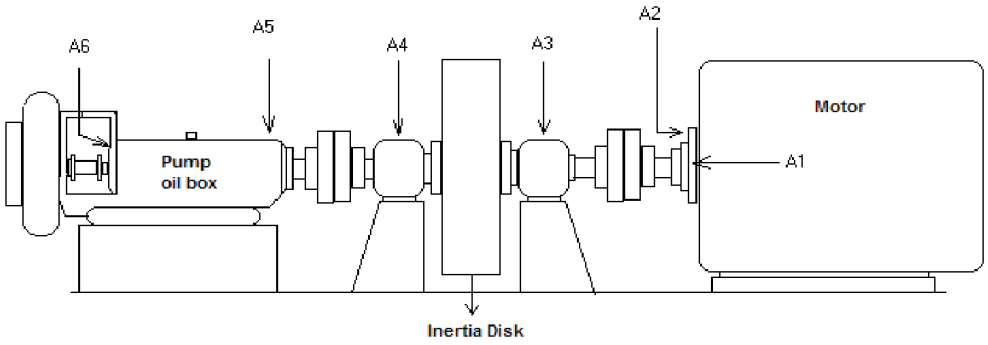

Figure 3 – Primary Pump - Components of the primary reactor pump with the points where accelerometers are installed.

Figure 3 illustrates the schematic representation and positions of the accelerometers: the transducer direction is horizontal in A1, vertical in A3, A4, and A5, and axial in A2 and A6.

The operational experience defined by specialists in (BENEVENUTI; TING, 2004a)for monitoring the primary circuit pumps consist of six distinct categories of mechanical issues. These encompass bearing problems (Dlr), bearing lubrication (Plb), mechanical clearances (Fg), impeller clearances (FgE), shaft misalignment problems (Db), and mass imbalance problems (Dl). In Table 2, we present the vibration parameters established for monitoring the primary pumps.

Table 2 - Vibration Parameters for Primary Pumps.

	A1	A2	A3	A4	A5	A6
Db	1°h, RMS_v	2°h, RMS_v	1°h, RMS_v	1°h, RMS_v	1°h, RMS_v	2°h, RMS_v
Dl	2°h,4°h, RMS_v	2°h, 4°h, RMS_v	2°h,4°h, RMS_v	2°h, 4°h, RMS_v	2°h, 4°h, RMS_v	2°h, 4°h, RMS_v
Fg	1°h, 2°h, 3°h, 4°h RMS_v	1°h, 2°h, 3°h,4°h RMS_v	1°h, 2°h, 3°h, 4°h RMS_v	1°h, 2°h, 3°h, 4°h RMS_v	1°h, 2°h, 3°h, 4°h RMS_v	1°h, 2°h, 3°h, 4°h RMS_v
FgE					4°h, 8°h, 12°h, 16°h	4°h, 8°h, 12°h, 16°h
Dlr	RMS_a.$Peak_a$, RMS_v		RMS_a.$Peak_a$, RMS_v	RMS_a.$Peak_a$, RMS_v	RMS_a.$Peak_a$, RMS_v	RMS_a.$Peak_a$, RMS_v
Plb	1°h, 2°h, 3°h, 4°h RMS_a.$Peak_a$, RMS_v		1°h, 2°h, 3°h, 4°h RMS_a.$Peak_a$, RMS_v	1°h, 2°h, 3°h, 4°h RMS_a.$Peak_a$, RMS_v	1°h, 2°h, 3°h, 4°h RMS_a.$Peak_a$, RMS_v	1°h, 2°h, 3°h, 4°h RMS_a.$Peak_a$, RMS_v

doi.org/10.32640/tasj.2024.6.20

TAS Journal, vol. 8, n. 3, p. 20
ISSN 2595-1521
SEPTEMBER 2024
carvalho@ipen.br

For each of the 6 pump accelerometers (A1, A2, A3, A4, A5, and A6), the following variables undergo monitoring:

- RMS in velocity (RMS_v),
- RMS in acceleration within the 1Hz to 5 KHz and 5KHz to 10 KHz ranges (RMS_a),
- Peak value in acceleration within the 1Hz to 5 KHz and 5KHz to 10 KHz ranges ($Peak_a$), and
- Velocity harmonics (1st, 2nd, 3rd, 4th, 8th, 12th, and 16th).

Methodology

Features Extraction. To implement an automated defect detection of pumps, we have utilized vibration levels from the accelerometers, measured in acceleration units (mm/s^2), acquired through a signal conditioner. Subsequently, the acquired signals have undergone processing in MATLAB, during which we have computed 12 distinct factors aimed to classify types of defects. This has involved employing the RMS and the Power Spectrum values for a thorough analysis.

First, the RMS of the acceleration signal is calculated for the 1Hz to 5kHz and 5kHz to 10kHz ranges, using Equation 1:

$$RMS_a = \sqrt{\frac{1}{T_2 - T_1}\int_{T_1}^{T_2} (f(t))^2 dt} \quad (1)$$

where:
f(t) = acceleration signal,
T = period of the signal.

Applying the discrete Fourier transform, peaks are found in the ranges of 1Hz to 5kHz and 5kHz to 10kHz, as Equation 2 shows:

$$X(k)_a = \frac{1}{N}\sum_{n=0}^{N-1} x(n) e^{-j\frac{2\pi}{N}kn} \quad (2)$$

where X(k)a is the discrete spectrum of the signal x(n) with period N.

The signal is then integrated using Equation 3:

doi.org/10.32640/tasj.2024.6.20

TAS Journal, vol. 8, n. 3, p. 20
ISSN 2595-1521
SEPTEMBER 2024
carvalho@ipen.br

$$v_i - v_{i-1} = \int_{t_{i-1}}^{t_i} \bar{a}(t)dt \approx \frac{T_s}{2}(\bar{a}_i + \bar{a}_{i+1}) \quad (3)$$

where:
v_i = velocity at instant i,
$\bar{a}(t)$ = average acceleration.

The RMS between 1Hz and 600Hz in velocity is calculated, as shown in Equation 4:

$$RMS_v = \sqrt{\frac{1}{T_2 - T_1}\int_{T_1}^{T_2} (f(t))^2 dt} \quad (4)$$

Finally, the discrete Fourier transform is applied to velocity, as shown in Equation 5:

$$X(k)_a = \frac{1}{N}\sum_{n=0}^{N-1} x(n)e^{-j\frac{2\pi}{N}kn} \quad (5)$$

where peaks are found at the following harmonics: 1st, 2nd, 3rd, 4th, 8th, 12th, and 16th.

Figure 4 shows a scheme of the Factor Extraction module based on accelerometer acquired signals. In this figure, we can see the RMS and Power spectrum extraction method from the pump accelerometer signals. This procedure was used for all the A1 to A6 accelerometers.

doi.org/10.32640/tasj.2024.6.20

TAS Journal, vol. 8, n. 3, p. 20
ISSN 2595-1521
SEPTEMBER 2024
carvalho@ipen.br

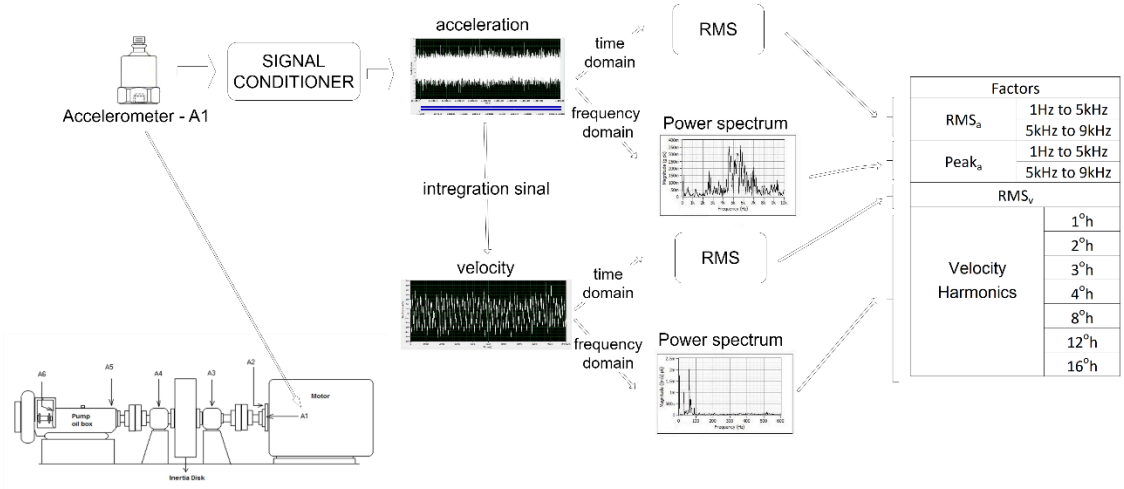

Figure 4 - Calculation of Factors from Vibration Signals – Calculation of RMS value of the signal and Power Spectrum (1st, 2nd, 3rd, 4th, 8th, 12th, and 16th harmonics) for a thorough analysis in acceleration and velocity.

These 12 factors are subsequently compared with the baseline vibration parameters, described in item 2.2, to construct the ANN input feature vectors. The comparison involves dividing the obtained values for each factor by their corresponding baseline values. After this division, the values used as input (features) for network training are obtained, consisting of 1 RMS of velocity, 2 RMS of acceleration, 2 peaks of acceleration, and 7 peaks of velocity (Table 3). Adhering to conventional practice, where alert levels are considered to be twice as high as reference levels, ratios exceeding 2 signify that the measurement surpasses the alert threshold, which indicates the beginning of defects in the pump. In Tables 3, we present the classes of defect types used in this work based on operational experience (refer to Table 2). These 7 classes are: encompass bearing problems (Dlr), bearing lubrication (Plb), mechanical clearances (Fg), impeller clearances (FgE), shaft misalignment problems (Db), mass imbalance problems (Dl), and if all the values are lower than 2, it means that there is no defects (SD).

Tables 3 - Characterization of Neural Network Features - Characterization for each type of defect based on operational experience

doi.org/10.32640/tasj.2024.6.20

TAS Journal, vol. 8, n. 3, p. 20
ISSN 2595-1521
SEPTEMBER 2024
carvalho@ipen.br

Defects Classes	RMS_v	RMS_a		$Peak_a$		$Peak_v$						
	1 - 600 Hz	1 - 5 kHz	5 - 10 kHz	1 - 5 kHz	5 - 10 Khz	1°h 30Hz	2°h 60Hz	3°h 90Hz	4°h 120Hz	8°h 240Hz	12°h 360Hz	16°h 480Hz
SD	< 2	< 2	< 2	< 2	< 2	< 2	< 2	< 2	< 2	< 2	< 2	< 2
Db	≥ 2	< 2	< 2	< 2	< 2	≥ 2	< 2	< 2	< 2	< 2	< 2	< 2
Fg	≥ 2	< 2	< 2	< 2	< 2	≥ 2	≥ 2	≥ 2	≥ 2	< 2	< 2	< 2
FgE	< 2	< 2	< 2	< 2	< 2	< 2	< 2	< 2	≥ 2	≥ 2	≥ 2	≥ 2
Dlr	≥ 2	≥ 2	≥ 2	≥ 2	≥ 2	< 2	< 2	< 2	< 2	< 2	< 2	< 2
Plb	≥ 2	≥ 2	≥ 2	≥ 2	≥ 2	≥ 2	≥ 2	≥ 2	≥ 2	< 2	< 2	< 2
Dl	≥ 2	< 2	< 2	< 2	< 2	< 2	≥ 2	< 2	≥ 2	< 2	< 2	< 2

Neural Network Architecture. Neural Network was trained using the MATLAB Deep Learning Toolbox (THE MATHWORKS INC, 2021). The implemented ANNs is a two-layer feedforward network using 12 inputs (12 features describe in Table 3), a sigmoid transfer function in the hidden layer and a softmax transfer function in the output layer. The Cross-Entropy was used to performance metric to be minimized by the algorithm. The neural network training involved varying the number of neurons in the hidden layer from 5 to 15. The lowest Cross-Entropy was achieved for 10 neurons. Figure 5 illustrates the variation of Cross-Entropy with the number of neurons. The number of output neurons was determined based on the elements in the target vector, corresponding to 2 or 3 categories depending on the types of defects.

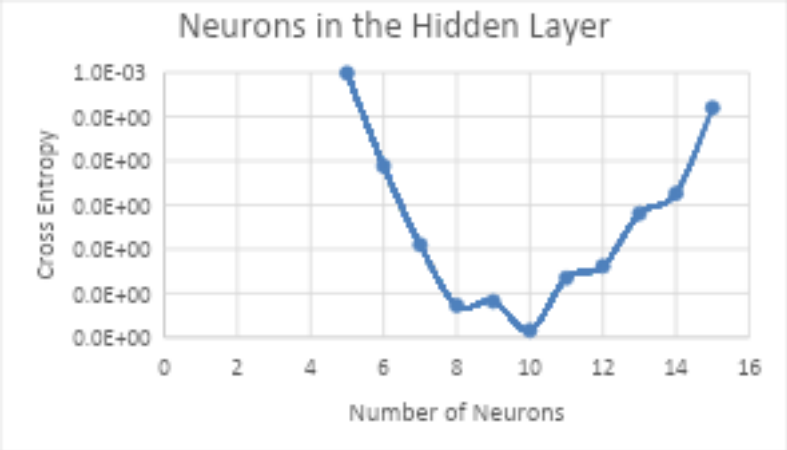

Figure 5 - Neural Network Performance - Neural Network Performance as a Function of the Number of Neurons in the Hidden Layer

The dataset was randomly divided into three sets: 70% for training, 15% for validation and 15% for testing. To assess network learning, three criteria were employed:

- Performance Graph,
- Confusion Matrix,
- Receiver Operating Characteristic (ROC) Curve.

doi.org/10.32640/tasj.2024.6.20

TAS Journal, vol. 8, n. 3, p. 20
ISSN 2595-1521
SEPTEMBER 2024
carvalho@ipen.br

ANNs Performance and Related Data. Between the years 2000 and 2003, during normal pump operation to establish reference levels and before events that necessitated the shutdown of the pumps for maintenance (BENEVENUTI; TING, 2004b), 104 measurements were conducted at 6 points on the pumps using the vibration signals from the SMV accelerometers. These signals were processed through a conditioner where they were amplified and filtered with a passband of 1Hz to 10kHz. Subsequently, they were digitized at a sampling rate of 30,000 points per second and finally stored in txt files. Between the years 2019 and 2020, we conducted 176 measurements using all the SMV accelerometers, shown in Figure 3, on the 2 pumps following the same strategy as in 2000 to 2003.

Data Collection: 2000-2003. The signals obtained between 2000 and 2003 were processed in MATLAB to extract the input features for the 6 ANNs trained.

Table 4 - Features and Output Classes of the Neural Network - Misalignment and bearing defects at point A6 of Pump A

RMS_v	RMS_a		$Peak_a$		$Peak_v$							Output Class
1–600 Hz	1–5 kHz	5–9 kHz	1–5 kHz	5–9 kHz	1°h	2°h	3°h	4°h	8°h	12°h	16°h	
1.15	0.00	0.00	0.00	0.00	3.85	1.20	1.41	0.67	1.32	0.74	1.15	100
1.15	0.00	0.00	0.00	0.00	4.41	0.85	3.96	0.70	1.37	0.78	1.01	100
1.21	0.00	0.00	0.00	0.00	6.22	3.16	1.06	1.13	0.50	0.72	1.01	100
1.15	0.00	0.00	0.00	0.00	3.68	2.94	4.10	0.85	0.96	1.02	1.33	100
1.08	0.00	0.00	0.00	0.00	4.07	0.89	2.12	0.87	0.73	1.20	1.44	100
1.07	1.14	0.95	1.19	1.07	2.52	1.31	0.93	0.74	0.28	0.92	0.73	100
1.11	1.03	0.93	1.19	1.15	2.08	2.46	1.60	0.80	0.19	0.82	0.76	100
0.99	1.17	0.58	1.13	0.74	1.40	0.39	1.10	0.88	1.84	1.45	0.84	1
0.95	0.80	1.01	0.75	0.89	0.76	0.85	0.97	1.05	0.55	1.25	0.92	1
0.90	0.84	1.04	0.78	0.93	0.80	1.31	1.00	1.25	1.48	1.23	0.90	1
0.89	0.90	1.03	1.81	1.04	0.52	0.92	2.00	0.89	1.58	0.85	0.80	1
0.94	1.05	1.02	3.09	1.15	1.40	1.23	0.88	1.12	1.32	0.91	0.71	10
1.14	1.08	1.03	2.59	1.04	3.28	1.38	2.40	0.95	0.97	0.35	0.37	10
1.17	2.70	1.11	5.38	3.30	2.12	1.46	1.20	1.03	1.42	1.26	1.06	10
1.32	3.21	1.18	6.25	3.96	2.00	1.08	0.63	0.97	1.26	1.31	1.04	10
3.07	4.86	1.36	14.50	6.52	1.00	1.23	1.00	1.15	0.94	1.15	0.76	10
1.04	2.00	1.20	2.32	2.60	1.22	0.52	0.42	0.64	1.81	1.22	1.00	10

Table 4 showcases the features and output classes of the neural network at point A6 of pump A. Factors exceeding alert levels (greater than 2) are highlighted in red. Each row corresponds to a vibration measurement. The initial 12 columns of the table (in green) present the features, while the last column displays the 3 binary digit output classes representing types of defects (in blue), where ‘001’ means that there are no defects (SD), ‘100’ identifies shaft misalignment problems (Db), and ‘010’ identifies bearing defects (Dlb).

doi.org/10.32640/tasj.2024.6.20

TAS Journal, vol. 8, n. 3, p. 20
ISSN 2595-1521
SEPTEMBER 2024
carvalho@ipen.br

The feature matrix shown in Table 4 forms a combined matrix with 13 columns: 12 columns for features and 1 column for output classes. The data were then presented to the neural networks to classify the defect types. The rows of Table 4 were randomly shuffled and presented to the neural networks to classify the defect types.

This procedure was repeated for all 5 datasets. The results of the 6 neural networks trained, one for each sensor (points A6(A), A5(A), A3(B), A4(B), A3(A) and A4(A)), indicating the pump and accelerometer (column 1), the total number of data, the number of defective data, and parameters for assessing network response. Best Validation Performance (BVP), Confusion Matrix and Receiver Operating Characteristic (ROC) curve are also described in Table 5. The BVP indicates whether the network has converged to the solution using the Cross-Entropy measure which was used as the cost function to be minimized by the algorithm. The Confusion Matrix shows whether the data were classified correctly. The ROC curves show how the false positive and true positive rates relate as the output threshold varies from 0 to 1.

Table 5 presents the measurement points in the first column, shown in Figure 3, with the corresponding pump indicated in parentheses. The second column lists the types of defects identified, while the third column provides the total number of data points. The fourth column details the number of data points per defect type. Subsequent columns display the network's performance metrics: the fifth column reports the BVP, and the following four columns show the classes identified by the network for training data (TrCM(70%)), validation data (VCM(15%)), test data (TCM(15%)), and all data combined (AllCM(100%)), with the number of classified instances provided in parentheses, the final four columns present the performance of the ROC curves for training data (TrROC), validation data (VROC), test data (TeROC), and all data combined (AllROC), where 'OK' denotes the absence of false positives and ‘FP’ denote a false positive.

An exception was noted in the case of point A5 of Pump A, concerning the classification of combined bearing and lubrication defects, where the Test Data Confusion Matrix (TeCM(15%)) displayed misclassifications, the six ANNs demonstrated consistent performance in defect classification.

Table 5 - Neural Network Response - Neural network responses for defect classification between 2000 and 2003

doi.org/10.32640/tasj.2024.6.20

TAS Journal, vol. 8, n. 3, p. 20
ISSN 2595-1521
SEPTEMBER 2024
carvalho@ipen.br

Point and Pump	Type of defect	Number of defect	Numbers of defect data	BVP	Confusion Matrix				ROC			
					TrCM 70%	VCM 15%	TeCM 15%	AllCM 100%	TrROC	VROC	TeROC	AllROC
A6(A)	Misalignment Bearing	17	7 6	$3.05x10^{-5}$	class1(5) class2(3) class3(3)	class1(1) class2(1) class3(1)	class1(1) class2(2) class3(0)	class1(7) class2(6) class3(4)	OK	OK	OK	OK
A5(A)	Bearing Lubrification	16	6	$2.42x10^{-7}$	class1(5) class2(7)	class1(1) class2(1)	class1(1) class2(1)	class1(6) class2(9)	OK	OK	FP	OK
A3(B)	Lubrification	16	6	$5.32x10^{-7}$	class1(7) class2(4)	class1(1) class2(1)	class1(1) class2(1)	class1(9) class2(6)	OK	OK	OK	OK
A4(B)	Lubrification	15	6	$4.82x10^{-8}$	class1(4) class2(8)	class1(1) class2(1)	class1(1) class2(1)	class1(6) class2(10)	OK	OK	OK	OK
A3(A)	Lubrificatio.	30	14	$1.58x10^{-8}$	class1(11) class2(9)	class1(3) class2(2)	class1(2) class2(3)	class1(16) class2(14)	OK	OK	OK	OK
A4(A)	Lubrification	28	10	0.02	class1(1) class2(9)	class1(2) class2(2)	class1(2) class2(2)	class1(14) class2(12)	OK	OK	OK	OK

Data Collection: 2019-2020

Between 2019 and 2020, the analysis was repeated using the same methodology as from 2000 to 2003, now using all accelerometers on the 2 pumps (12 points). The 12 ANNs results for defect classification are they were presented in Table 6, in the same manner as they were presented in Table 5.

The observed performance of the networks in defect classification was generally consistent. Exceptions were noted at points A1 of Pump A and A2 of Pump B in the classification of clearance defects, where Receiver Operating Characteristic (ROC) curves exhibited false positives (FP) due to one of the classes having zero data.

Table 6 - Neural Network Response - Neural network responses for defect classification between 2019 and 2020

doi.org/10.32640/tasj.2024.6.20

TAS Journal, vol. 8, n. 3, p. 20
ISSN 2595-1521
SEPTEMBER 2024
carvalho@ipen.br

Point and Pump	Types of defect	Number of defect	Number of defect data	BVP	Confusion Matrix				ROC			
					TrCM 70%	VCM 15%	TeCM 15%	AIICM 100%	TrROC	VROC	TeROC	AIIROC
A1(A)	Cleareance	16	5	$3.18x10^{-8}$	class1(5) class2(7)	class1(0) class2(2)	class1(0) class2(2)	class1(5) class2(11)	OK	class1 FP	class1 FP	OK
A2(A)	Cleareance	18	12	$3.37x10^{-7}$	class1(9) class2(3)	class1(1) class2(1)	class1(2) class2(1)	class1(12) class2(6)	OK	OK	OK	OK
A3(A)	Lubrification	16	12	$3.80x10^{-7}$	class1(0) class2(2)	class1(1) class2(1)	class1(1) class2(1)	class1(12) class2(4)	OK	OK	OK	OK
A4(A)	Cleareance	24	12	$1.52X10^{-6}$	class1(8) class2(8)	class1(3) class2(1)	class1(1) class2(3)	class1(12) class2(12)	OK	OK	OK	OK
A5(A)	Mass imbalance	21	10	$3.50X10^{-7}$	class1(7) class2(9)	class1(1) class2(2)	class1(2) class2(1)	class1(10) class2(11)	OK	OK	OK	OK
A6(A)	Lubrification	18	12	$2.20x10^{-6}$	class1(8) class2(4)	class1(2) class2(1)	class1(2) class2(1)	class1(2) class2(6)	OK	OK	OK	OK
A1(B)	Cleareance	17	5	0.039	class1(2) class2(9)	class1(2) class2(1)	class1(1) class2(2)	class1(5) class2(12)	OK	OK	OK	OK
A2(B)	Clereance	15	2	$1.40x10^{-7}$	class1(9) class2(2)	class1(2) class2(0)	class1(2) class2(0)	class1(9) class2(6)	OK	class2 FP	class2 FP	OK
A3(B)	Lubrification	15	6	$4.82x10^{-8}$	class1(4) class2(8)	class1(1) class2(1)	class1(1) class2(1)	class1(13) class2(2)	OK	OK	OK	OK
A4(B)	Bearing	18	9	$6.61x10^{-8}$	class1(5) class2(7)	class1(7) class2(1)	class1(2) class2(1)	class1(9) class2(9)	OK	OK	OK	OK
A5(B)	Impeller Cleareance Bearing	19	9	$3.59x10^{-8}$	class1(6) class2(7)	class1(7) class2(1)	class1(2) class2(1)	class1(9) class2(10)	OK	OK	OK	OK
A6(B)	Impeller Cleareance	14	8	$7.53x10^{-6}$	class1(6) class2(4)	class1(1) class2(1)	class1(1) class2(1)	class1(8) class2(6)	OK	OK	OK	OK

Results and Discussion. Based on operational experience with the primary circuit pumps of the reactor, 12 features were identified for the classification of defects in these pumps. Using vibration measurement data collected between 2000 and 2003, ANNs were trained for each sensor, demonstrating that the data indicated defects previously confirmed by specialists. The ANNs correctly classified the defects in the pumps, as verified by historical data from that period. By inputting new data collected between 2019 and 2020 into the ANNs, the defect predictions were confirmed by subsequent maintenance, proving the model's effectiveness. Based on these results, it is confirmed that ANNs are efficient in classifying defects in the primary circuit pumps of the reactor.

The technique, utilizing the 12 features, can be expanded as new features are evidenced, providing even more precise defect classification. Other features that can be considered for defect characterization include the envelope technique and the analysis of the harmonics of the characteristic frequencies of bearing defects, as well as the characterization of the inter-harmonics of the pump's rotation frequencies for clearance problems.

doi.org/10.32640/tasj.2024.6.20

This conclusion highlights the consistency and adaptability of the defect classification technique using ANNs, supported by both historical and recent data, and suggests pathways for future improvements in the methodology. It is desirable to use a broader set of data to train a more general ANN capable of classifying 5 defect types simultaneously. However, this is not possible due the shortage of historical data.

Recent studies have demonstrated that the combination of AI models, such as Artificial Neural Networks (ANN), Support Vector Machines (SVM), and K-Nearest Neighbors (KNN) can improve accuracy in detecting faults in critical mechanical systems (SANTOS, 2024). In the context of predicting failures in research reactor pumps, applying ensemble AI models can be a promising direction for enhancing monitoring and diagnostic techniques. This approach can reduce incorrect diagnoses and increase system robustness, enabling more efficient predictive maintenance.

References

(1) ABDISA; W. T.; HARD, H. A Neural Network Based Motor Bearing Fault Diagnosis Algorithm and its Implementation on Programmable Logic Controller. **International Journal of Intelligent Systems and Applications**, v. 11, n. 10, p. 1–14, 8 out. 2019.
(2) AL TOBI, M. et al. Using MLP-GABP and SVM with wavelet packet transform-based feature extraction for fault diagnosis of a centrifugal pump. **Energy Science and Engineering**, v. 10, n. 6, p. 1826–1839, 1 jun. 2022.
(3) ALBLAWI, A. Fault diagnosis of an industrial gas turbine based on the thermodynamic model coupled with a multi feedforward artificial neural networks. **Energy Reports**, v. 6, p. 1083–1096, 1 nov. 2020.
(4) BENEVENUTI, É. L.; TING, D. K. S. **Vibration Monitoring and Diagnosis at the IEA-R1 Nuclear Research Reactor**, 2004a.
(5) BENEVENUTI, É. L.; TING, D. K. S. **Metodologia para monitoração e diagnóstico de vibração das bombas moto-operadas do circuito primário de refrigeração do Reator IEA-R1**. São Paulo: Universidade de São Paulo - USP, 2004b.
(6) DURRANT, A.; LEONTIDIS, G.; KOLLIAS, S. 3D convolutional and recurrent neural networks for reactor perturbation unfolding and anomaly detection. **EPJ Nuclear Sciences & Technologies**, v. 5, p. 20, 2019.
(7) EL-SEFY, M. et al. Artificial neural network for predicting nuclear power plant dynamic behaviors. **Nuclear Engineering and Technology**, v. 53, n. 10, p. 3275–3285, 1 out. 2021.
(8) GARCIA-BRACAMONTE, J. E. et al. An Approach on MCSA-Based Fault Detection Using Independent Component Analysis and Neural Networks. **IEEE Transactions on Instrumentation and Measurement**, v. 68, n. 5, p. 1353–1361, 1 maio 2019.

doi.org/10.32640/tasj.2024.6.20

(9) GLOWACZ, A.; GLOWACZ, W. Vibration-Based Fault Diagnosis of Commutator Motor. **Shock and Vibration**, v. 2018, 2018.

(10) HAGGAG, S.; ADLY, A.; ZAKY, M. Artificial Neural Network Model for Fault Diagnosis of Rotating Machine in ETRR-2 Research Reactor. **Arab Journal of Nuclear Sciences and Applications**, v. 55, n. 3, p. 55–61, 14 mar. 2022.

(11) HOANG, D. T.; KANG, H. J. Rolling element bearing fault diagnosis using convolutional neural network and vibration image. **Cognitive Systems Research**, v. 53, p. 42–50, 1 jan. 2019.

(12) HOU, L. et al. A fault diagnosis model of marine diesel engine cylinder based on modified genetic algorithm and multilayer perceptron. **Soft Computing**, v. 24, n. 10, p. 7603–7613, 1 maio 2020.

(13) IANNACE, G.; CIABURRO, G.; TREMATERRA, A. Fault diagnosis for UAV blades using artificial neural network. **Robotics**, v. 8, n. 3, 1 set. 2019.

(14) INTERNATIONAL ATOMIC ENERGY AGENCY. **On-line Monitoring of Instrumentation in Research Reactors**. Vienna: 2017.

(15) INTERNATIONAL ORGANIZATION FOR STANDARDIZATION. **Mechanical vibration — Measurement and evaluation of machine vibration — Part 1: General guidelines**. [s.l: s.n.].

(16) JIN, Z. et al. An intelligent fault diagnosis method of rolling bearings based on Welch power spectrum transformation with radial basis function neural network. **JVC/Journal of Vibration and Control**, v. 26, n. 9–10, p. 629–642, 1 maio 2020.

(17) KELEŞOĞLU, C.; KÜÇÜK, H.; DEMETGÜL, M. Fault Diagnosis of Bevel Gears Using Neural Pattern Recognition and MLP Neural Network Algorithms. **International Journal of Precision Engineering and Manufacturing**, v. 21, n. 5, p. 843–856, 1 maio 2020.

(18) KHOUALDIA, T. et al. Optimized multi layer perceptron artificial neural network based fault diagnosis of induction motor using vibration signals. **Diagnostyka**, v. 22, n. 1, p. 65–74, 2021.

(19) LI, F.; PANG, X.; YANG, Z. Motor current signal analysis using deep neural networks for planetary gear fault diagnosis. **Measurement: Journal of the International Measurement Confederation**, v. 145, p. 45–54, 1 out. 2019.

(20) LI, H. et al. Fault diagnosis for machinery based on feature extraction and general regression neural network. **International Journal of System Assurance Engineering and Management**, v. 9, n. 5, p. 1034–1046, 1 out. 2018.

(21) LIU, H. et al. Fault diagnosis of rolling bearings with recurrent neural network-based autoencoders. **ISA Transactions**, v. 77, p. 167–178, 1 jun. 2018.

(22) LU, Q. et al. An Improved Fault Diagnosis Method of Rotating Machinery Using Sensitive Features and RLS-BP Neural Network. **IEEE Transactions on Instrumentation and Measurement**, v. 69, n. 4, p. 1585–1593, 1 abr. 2020.

(23) MARTÍNEZ-MORALES, J. D.; PALACIOS-HERNÁNDEZ, E. R.; CAMPOS-DELGADO, D. U. Multiple-fault diagnosis in induction motors through support vector machine classification at variable operating conditions. **Electrical Engineering**, v. 100, n. 1, p. 59–73, 1 mar. 2018.

doi.org/10.32640/tasj.2024.6.20

(24) SANTOS, B. J. ; C. I. A. A. Intelligent reflux and suction detection system for ventricular assist devices: in silico study. **Research on Biomedical Engineering**, p. 8, 10 dez. 2024.
(25) SAUFI, S. R. et al. **An intelligent bearing fault diagnosis system: A review**. 2018. Disponível em: <https://doi.org/10.1051/matecconf/20192>
(26) SIANO, D.; PANZA, M. A. **Diagnostic method by using vibration analysis for pump fault detection**. Energy Procedia. **Anais**...Elsevier Ltd, 2018.
(27) TAO, H. et al. An unsupervised fault diagnosis method for rolling bearing using STFT and generative neural networks. **Journal of the Franklin Institute**, v. 357, n. 11, p. 7286–7307, 1 jul. 2020.
(28) THE MATHWORKS INC. **MATLAB Version: 9.10.0.1602886 (R2021a)**. Natick, Massachusetts, 2021.
(29) THE MATHWORKS INC. **MATLAB - Deep Learning Toolbox** . Natick, Massachusetts, 2021.
(30) WANG, Z. Y.; LU, C.; ZHOU, B. Fault diagnosis for rotary machinery with selective ensemble neural networks. **Mechanical Systems and Signal Processing**, v. 113, p. 112–130, 1 dez. 2018.
(31) XU, X. et al. Application of neural network algorithm in fault diagnosis of mechanical intelligence. **Mechanical Systems and Signal Processing**, v. 141, 1 jul. 2020.
(32) ZHAO, C. et al. **An EEMD and convolutional neural network based fault diagnosis method in intelligent power plant**. Proceedings Chinese Automation Congress (CAC2019) . **Anais**...Hangzhou - China: 28 jul. 2020a.
(33) ZHAO, W. et al. On the use of artificial neural networks for condition monitoring of pump-turbines with extended operation. **Measurement: Journal of the International Measurement Confederation**, v. 163, 15 out. 2020b.
(34) ZUO, L. et al. A spiking neural network-based approach to bearing fault diagnosis. **Journal of Manufacturing Systems**, v. 61, p. 714–724, 1 out. 2021.

The ORCID of all authors:
CARVALHO, M. R.: 0009-0006-1537-4998
DIAS, M. S.: 0000-0003-2478-5757
DE MESQUITA, R. N.: 0000-0002-5355-0925
POVEDA, P. F.: 0000-0002-2963-2007

doi.org/10.32640/tasj.2024.6.20